Optics Communications 339 (2015) 209–215

Contents lists available at ScienceDirect

Optics Communications

journal homepage: www.elsevier.com/locate/optcom

Electromagnetically induced transparency with Laguerre–Gaussian modes in ultracold rubidium

T.G. Akin, S.P. Krzyzewski, A.M. Marino, E.R.I. Abraham *

Homer L. Dodge Department of Physics and Astronomy, University of Oklahoma, 440 W. Brooks St. Norman, OK 73019, USA

ARTICLE INFO

Article history:
Received 15 August 2014
Received in revised form
5 November 2014
Accepted 12 November 2014
Available online 17 November 2014

Keywords:
Laguerre–Gaussian mode
Electromagnetically induced transparency
Coherent control
Diffractive optics

ABSTRACT

We demonstrate electromagnetically induced transparency with the control laser in a Laguerre–Gaussian mode. The transmission spectrum is studied in an ultracold gas for the D2 line in both ^{85}Rb and ^{87}Rb, where the decoherence due to diffusion of the atomic medium is negligible. We compare these results to a similar configuration, but with the control laser in the fundamental laser mode. We model the transmission of a probe laser under both configurations, and we find good agreement with the experiment. We conclude that the use of Laguerre–Gaussian modes in electromagnetically induced transparency results in narrower resonance linewidths as compared to uniform control laser intensity. The narrowing of the linewidth is caused by the spatial distribution of the Laguerre–Gaussian intensity profile.

1. Introduction

Electromagnetically induced transparency (EIT) is an optical technique used to manipulate quantum states of atoms and photons [1]. A control laser modifies the absorption profile of a probe laser, causing coherent destructive interference of excitation pathways of the atom. The result is an increased transmission of the probe laser tuned to an atomic resonance where absorption is otherwise expected. Applications of EIT range from coherent storage of light in the atomic medium for quantum information storage [2,3], nonlinear optics [4], and lasing without population inversion [5].

Initial spectroscopic studies of EIT were performed in an atomic gas at room temperature [6]. Large laser powers can overcome the Doppler broadening, but cause homogeneous line broadening, though specific Doppler-free techniques produce EIT signals in a room temperature gas with moderate laser powers [7–10]. Alternatively, experiments that produce ultracold samples of atomic gases result in Doppler-broadening smaller than the natural linewidth of the atomic transition. The reduced transverse motion of cold atoms also suppresses the decoherence due to diffusion. Ultracold gases also offer high densities, typically in the range from 10^9 to 10^{12} cm^{-3}. For these reasons, EIT has been extensively studied in this environment [11–15].

One consequence of EIT is the slowing of light in an atomic sample. The destructive interference of excitation pathways in EIT leads to a sub-natural linewidth transmission feature. There is no theoretical minimum to the linewidth, which is only limited by experimental constraints, such as background magnetic fields, laser linewidth, atomic collisions, and other homogeneous broadening [1]. Slow light results from enhancement of the slope of the dispersion in the frequency range near the EIT resonance. Lowering of the intensity of the control field leads to narrowing of the EIT linewidth and results in the decrease of probe group velocity. Speeds many orders of magnitude less than c have been achieved in an ultracold gas [16] and in room temperature gases [17,18]. A slowed probe pulse propagating through the medium can be coherently stored in and retrieved from the atoms by adiabatically switching the control laser off and on [2,3].

Incorporation of a laser propagating in a Laguerre–Gaussian LG_p^l mode to EIT is of considerable interest. The azimuthal winding phase ($e^{il\phi}$) leads to quantized orbital angular momentum (OAM) of $l\hbar$ per photon. A probe laser carrying OAM generates a manifold of information degrees of freedom, allowing multi-dimensional quantum computing and encryption [19]. Storage of LG_p^l mode probe pulses in gases has been demonstrated in both room temperature gases [20–23], and in ultracold gases [24–27]. The OAM forces the intensity to go to zero at the center, and the additional p radial nodes give rise to “doughnut” shaped beams, or even concentric ring intensity patterns and a spatially varying Rabi frequency.

* Corresponding author. Fax: +1 405 325 7557.
E-mail address: abraham@nhn.ou.edu (E.R.I. Abraham).

http://dx.doi.org/10.1016/j.optcom.2014.11.049
0030-4018/

A control laser with a large Rabi frequency (as compared to the decoherence rates) increases the signal contrast of the EIT feature, while a small Rabi frequency results in a narrower EIT resonance. Placing a control laser in an LG_p^l mode, and aligning the probe laser to the central node cause most of the probed atoms to experience a low control field, resulting in a narrowing of the EIT resonance. Then, the control laser power can be increased, improving the signal. Previously, sub-natural linewidths were observed in the EIT transmission spectra using an LG_0^1 control beam in room temperature gases [28,29]. Remarkably, the LG_0^1 control laser reduced the EIT linewidth by a factor of 2 as compared to a similar experiment with the control in a Gaussian mode. It was proposed in ref. [29] that the OAM of the control beam could decrease the decoherences due to transit effects of the room temperature gas. However, they show that increasing OAM does not increase the narrowing and argue that the reduction in EIT linewidth is entirely due to the spatial dependence of the control Rabi frequency.

We measure EIT transmission spectra using an LG_0^1 laser mode in ultracold atoms prepared in a magneto-optical trap (MOT). We find narrowing of the EIT resonance, and in the ultracold system transit decoherences are negligible. We measure EIT linewidths with the control beam in the LG_0^1 mode and the probe in the fundamental Gaussian mode for four different EIT configurations of the D2 line for both ^{85}Rb and ^{87}Rb. We compare this data with EIT spectra where both the probe and the control lasers are in the fundamental Gaussian mode. A theoretical model is used to analyze each configuration. We use a density matrix formalism for a six level system composing the two ground-state hyperfine levels and the four excited-state hyperfine levels of the D2 transition in ^{85}Rb and ^{87}Rb. We model the fields as plane waves when the control is in the fundamental mode, and include the spatially varying Rabi frequency when the control is in the LG_0^1 mode [30,28]. A transmission spectrum is generated from the steady-state solutions of the density matrix equations. We find good agreement between the model and the experiment. For both theory and experiment, we observe narrower EIT resonance features with the control laser in the LG_0^1 mode than with the control laser in the Gaussian mode.

2. Experimental design

The experimental set-up for our MOT is shown in Fig. 1 and is similar to that found in [31]. The trapping laser is a low-powered external-cavity diode laser locked ≃15 MHz to the red of the $|F=3\rangle \rightarrow |F'=4\rangle$ ($|F=2\rangle \rightarrow |F'=3\rangle$) atomic transition in ^{85}Rb (^{87}Rb) as shown in Fig. 2. It is amplified by a tapered amplifier in the master-oscillator power-amplifier configuration and spatially filtered using a polarization maintaining single-mode fiber. The output of the fiber has a power of 175 mW, and is telescoped to a $1/e^2$ beam diameter of 2.5 cm. It is further split into six beams, three of the beams are directed toward the cell along three orthogonal axes, and the other three beams counter-propagate along these axes with opposite circular polarizations. The repumping laser is locked on resonance with the $|F=2\rangle \rightarrow |F'=3\rangle$ ($|F=1\rangle \rightarrow |F'=2\rangle$) atomic transition in ^{85}Rb (^{87}Rb) as shown in Fig. 2. The laser has a power of 10 mW, is telescoped to a $1/e^2$ diameter of 2.5 cm, and is directed through a polarizing beam-splitter (PBS) to co-propagate with the trapping laser. The MOT routinely traps 10^8 atoms at a temperature of 50 μK. The density distribution of the atoms is Gaussian with a peak density of $(1-5)\times 10^{10}$ cm^{-3} and $1/e^2$ radius of ≃2 mm. Three sets of Helmholtz coils eliminate the effects of background magnetic fields.

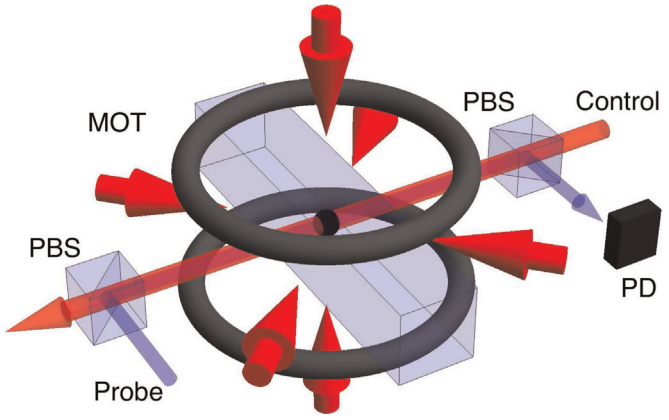

Fig. 1. Schematic of the ultracold EIT experimental apparatus. The magneto-optical trap (MOT) consists of a pair of anti-Helmholtz coils, six orthogonal and counter-propagating trapping lasers, and a repumping laser (co-propagating with the trapping laser). The control laser is indicated by the transparent red beam. The probe laser is indicated by the transparent blue beam. The control and the probe have orthogonal linear polarizations, and are combined/separated using polarizing beam-splitters (PBS), and are counter-propagating. The probe is imaged on a photodiode (PD). (For interpretation of the references to color in this figure caption, the reader is referred to the web version of this paper.)

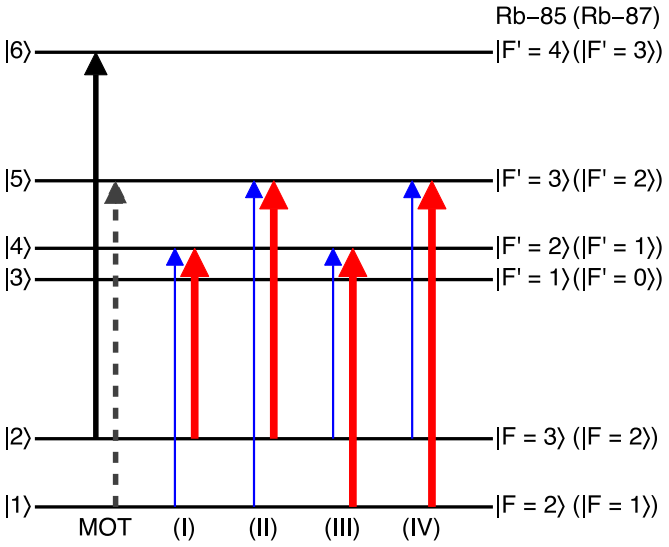

Fig. 2. The six hyperfine states for the D2 transition in ^{85}Rb (^{87}Rb). The solid black arrow corresponds to the trapping laser, and the gray dashed arrow corresponds to the repumping laser in our magneto-optical trap (MOT). Four EIT configurations on the D2 transition are indicated with Roman numerals. The thin blue arrows represent the probe laser, while the thick red arrows represent the control laser. (For interpretation of the references to color in this figure caption, the reader is referred to the web version of this paper.)

The probe laser is also an external cavity diode laser. The frequency of the probe is scanned 150–500 MHz across the resonances indicated in Fig. 2 by ramping the voltage across a piezoelectric transducer attached to the grating that serves as the output coupler on the external cavity [32]. The probe laser is shuttered using an acoustic optical modulator (AOM), and is spatially filtered using a polarization maintaining fiber optic cable. The power after the fiber is approximately 10 μW and is linearly polarized. The beam is overlapped with the control laser with a PBS and directed through the center of the MOT (Fig. 1) with a $1/e^2$ radius of 430 μm. After passing through the ultracold atomic sample, the probe is separated from the counter-propagating control laser with another PBS and is focused onto a Thorlabs DET200 photodiode (PD) that records the EIT transmission spectrum.

The control laser is locked near the transition indicated in each of the four configurations shown in Fig. 2. We use a dichroic atomic vapor laser lock (DAVLL) [33], resulting in a frequency stability of ≃1.5 MHz. The laser is shuttered using an AOM, and spatially filtered using a polarization maintaining fiber optic cable. The output of the fiber is ≃10 mW. To select an appropriate Rabi frequency, we attenuate the power using a set of neutral density filters. The polarization of the control laser is orthogonal to the probe, and the beam is directed counter-propagating to the probe using a PBS (Fig. 1). At the MOT, the control laser has a $1/e^2$ radius of 1.1 mm when in the Gaussian mode and 270 μm when in the LG_0^1 mode. The LG_0^1 mode beam waist is smaller than the Gaussian mode waist to increase the peak intensity of the control beam. This is necessary to counteract the loss of laser power after converting the Gaussian mode to the LG_0^1 mode. Since the control laser is a diode laser, the generation of LG_p^l modes must occur external to the cavity. We shape the control laser into an LG_0^1 mode using diffractive optics [34]. A diffractive optic has microscopic structures etched into the surface using lithography techniques. Using Huygens' principle, the initial Gaussian mode of the diode laser can be transformed into an LG_p^l wavefront using two optics. One optic transforms the intensity profile, and the second optic controls the winding phase. Diffractive optics can create higher order LG_p^l modes with high mode purity [34].

The EIT sequence is controlled by a Hewlett-Packard 8175A Digital Signal Generator. Digital pulses shutter the AOMs on the probe, control, and the repump lasers, and control the current flowing through the MOT coils, which can be turned off in 10 μs. Initially, the MOT is held in a steady state for 96 ms, and the probe and the control lasers are off. Next, the magnetic field is switched off and we optically pump the atoms for 1 ms. The optical pumping procedure depends on the EIT configuration. For configurations (I) and (II), the repump laser is switched off while the trapping laser optically pumps all the atoms into the lower hyperfine ground-state. For configurations (III) and (IV), the repump laser stays on to optically pump any atoms from the lower hyperfine ground state to the upper hyperfine ground state. After optical pumping, the control and probe lasers perform the EIT spectroscopy. The control laser pulse is 3 ms and precedes the probe laser pulse by 1 ms to prepare the atoms for EIT. The probe laser is on for 2 ms, during which it scans between 150 and 500 MHz, depending on the EIT configuration studied. A photodiode detects the probe transmission and the signal is read on a TDS-3054 oscilloscope. The entire procedure takes 0.1 s, and we cycle continuously so that the MOT is approximately in a steady state.

3. Theoretical model

We model the experiment using a density matrix formalism [1,28,30,35]. The density matrix operator is given by $\hat{\rho} = |\psi\rangle\langle\psi|$, where $|\psi\rangle$ is the atomic state vector. We consider a six level atom with two levels belonging to the hyperfine levels in the $^2S_{1/2}$ state, and the remaining four levels belonging to the hyperfine levels in the $^2P_{3/2}$ state in rubidium. Fig. 2 shows these states and identifies the four EIT configurations we model.

The total Hamiltonian for the atom interacting with an electric field is $\widehat{H} = \widehat{H}_0 + \widehat{H}_I$, where the Hamiltonian describing the atomic system is given by

$$\widehat{H}_0 = \sum_{n=1}^{6} \hbar\omega_n |n\rangle\langle n|, \tag{1}$$

where $\hbar\omega_n$ is the energy of the nth level. For each configuration shown in Fig. 2, the Hamiltonian describing the interactions with the electric field can be written as

$$\widehat{H}_I = \hbar\Omega_{c,kl}(r)e^{i(\omega_c t - k_c z + l_c\phi)}|k\rangle\langle l| + \text{h. c.} + \sum_{j=i+2}^{i+4}\left[\hbar\Omega_{p,ij}(r)e^{i(\omega_p t + k_p z)}|i\rangle\langle j| + \text{h. c.}\right], \tag{2}$$

where i and j are the level numbers of the states coupled by the probe laser, and k and l correspond to the level numbers of the states coupled by the control laser. Table 1 summarizes the level designations that are fixed for each configuration. The j index is summed over levels for allowed transitions. In Eq. (2), ω_p is the angular frequency and k_p is the wave number of the probe laser.

Table 1
Appropriate indices for our level scheme.

Index	(I)	(II)	(III)	(IV)
i	1	1	2	2
k	2	2	1	1
l	4	5	4	5

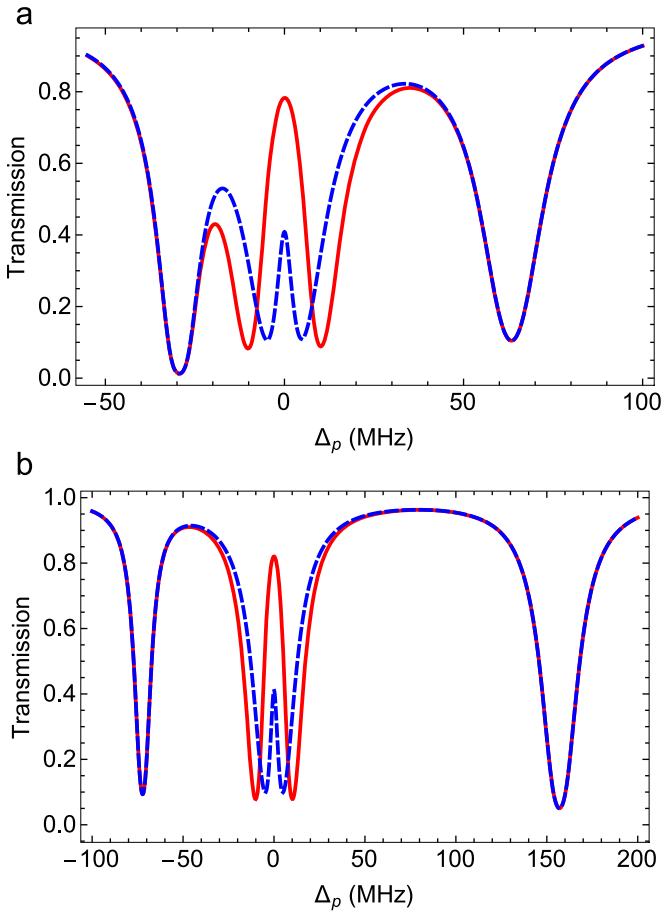

Fig. 3. Theoretical curves of the transmission of the probe laser for configuration (I) EIT in (a) ^{85}Rb and (b) ^{87}Rb. The solid red curve indicates the control laser is in a Gaussian mode, and the dashed blue curve indicates the control laser in an LG_0^1 mode. In both scenarios, the control Rabi frequency is the same ($\Omega_{0c,kl} = 20$ MHz). The linewidth of the control laser is assumed to be $\gamma_c = 1$ MHz, the linewidth of the probe laser is set $\gamma_p = 0.1$ MHz, the number density is set to $N = 5 \times 10^{10}$ cm^{-3}, and the detuning of the control laser is set to $\Delta_c = 0$. Due to the spatial dependence of a LG_0^1 mode laser, the model predicts that the EIT resonance with the same $\Omega_{0c,kl}$ is narrower for a control laser in the LG_0^1 mode than for a control laser in the Gaussian mode. (For interpretation of the references to color in this figure caption, the reader is referred to the web version of this paper.)

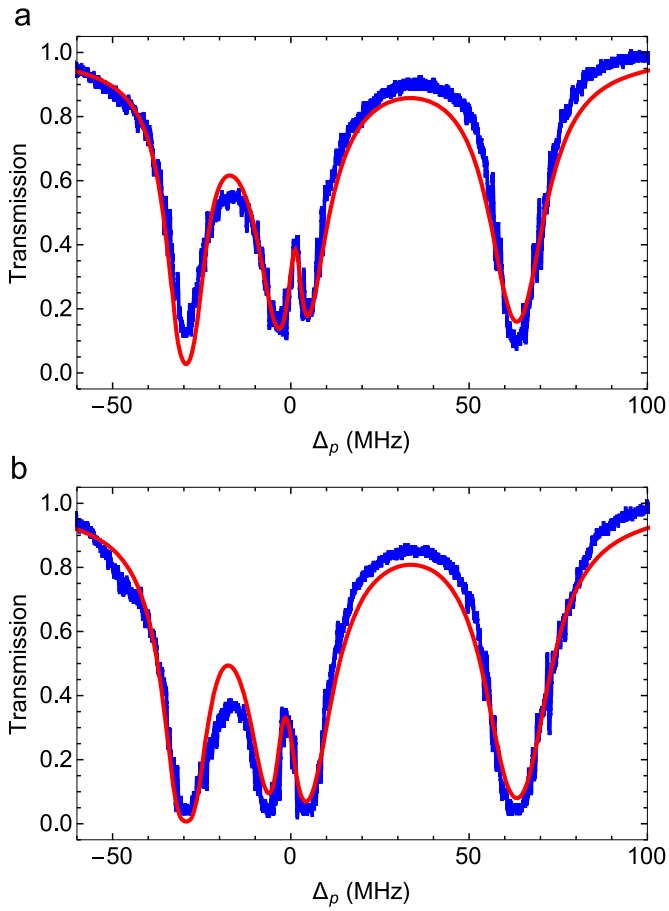

Fig. 4. The transmission spectrum for a probe laser scanning over the transitions $|F=2\rangle \rightarrow |F'=1, 2, 3\rangle$ in ^{85}Rb. The blue curve is the observed signal, and the red curve is the model. (a) The control laser is in the LG_0^1 mode 1.4 MHz above the $|F=3\rangle \rightarrow |F'=2\rangle$ transition with $\Omega_{0c,32}=16$ MHz. (b) The control laser is in the Gaussian mode 1.8 MHz below the $|F=3\rangle \rightarrow |F'=2\rangle$ transition with $\Omega_{0c,32}=9.5$ MHz. (For interpretation of the references to color in this figure caption, the reader is referred to the web version of this paper.)

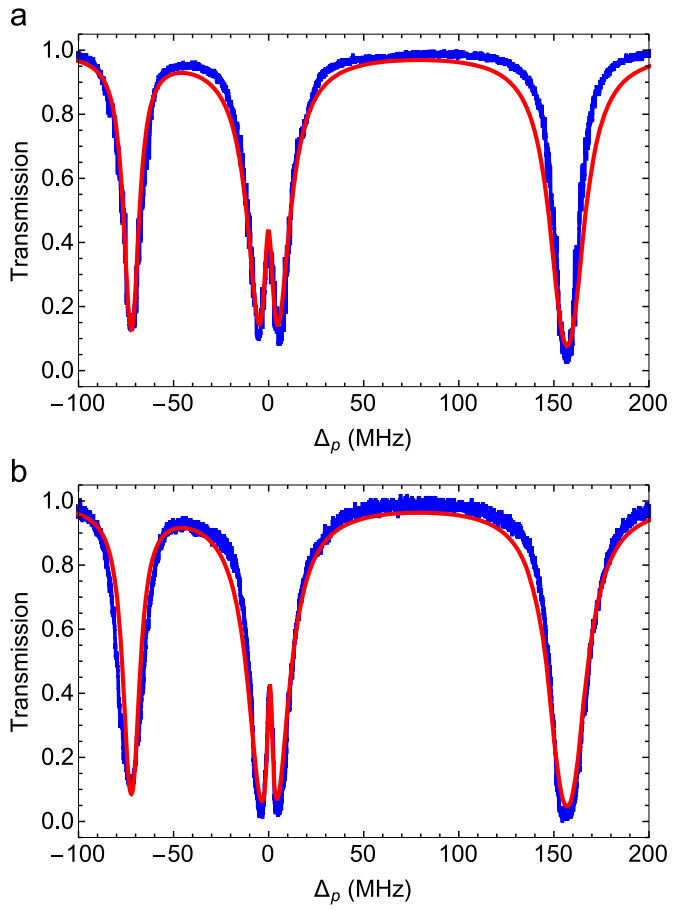

Fig. 5. The transmission spectrum for a probe laser scanning over the transitions $|F=1\rangle \rightarrow |F'=0, 1, 2\rangle$ in ^{87}Rb. The blue curve is the observed signal, and the red curve is the model. (a) The control laser is in the LG_0^1 mode 0.1 MHz below the $|F=2\rangle \rightarrow |F'=1\rangle$ transition with $\Omega_{0c,21}=20$ MHz. (b) The control laser is in the Gaussian mode 0.7 MHz above the $|F=2\rangle \rightarrow |F'=1\rangle$ transition with $\Omega_{0c,21}=6.7$ MHz. (For interpretation of the references to color in this figure caption, the reader is referred to the web version of this paper.)

Likewise, ω_c is the angular frequency, k_c is the wave number, and ℓ_c is the azimuthal charge of the control laser. The Rabi frequencies for the probe and control lasers are defined as

$$\Omega_{p,ij}(r) = -\frac{d_{ij}\mathcal{E}_p(r)}{\hbar},\ \Omega_{c,kl}(r) = -\frac{d_{kl}\mathcal{E}_c(r)}{\hbar}. \tag{3}$$

The dipole matrix elements, $d_{mn}=\langle m|\hat{\epsilon}\cdot\hat{d}|n\rangle$, of dipole-allowed transitions are taken from refs. [36,37]. The rest are set to zero. $\mathcal{E}_p(r)$ and $\mathcal{E}_c(r)$ are the possibly spatially dependent amplitudes of the probe and the control lasers, respectively [38]:

$$\mathcal{E}_p(r) = \mathcal{E}_{0,p} \quad \text{Probe in Gaussian mode} \mathcal{E}_c(r) = \begin{cases} \mathcal{E}_{0,c}\left(\frac{\sqrt{2}r}{w_{0,c}}\right)e^{-r^2/w_{0,c}^2} & \text{Control in } LG_0^1 \text{ mode} \\ \mathcal{E}_{0,c} & \text{Control in Gaussian mode} \end{cases} \tag{4}$$

where $\mathcal{E}_{0,p}$ and $\mathcal{E}_{0,c}$ are constants, and $w_{0,c}$ is the waist of the control laser. We define Rabi frequency constants, $\Omega_{0p,ij}=-d_{ij}\mathcal{E}_{0,p}/\hbar$ for the probe laser and $\Omega_{0c,kl}=-d_{kl}\mathcal{E}_{0,c}/\hbar$ for the control laser. These constants are used to compare different configurations of LG_0^1 and Gaussian control beams to be consistent with refs. [28,29]. To verify the plane-wave approximation for the Gaussian modes, we evaluated our model with the inclusion of the Gaussian spatial variation. To the precision of our experiment, we saw no effect on the calculations.

We use two unitary transformations on both the density matrix operator and the Hamiltonian. We transform into the rotating frame using the following unitary transformation:

$$\hat{U}_1 = \exp\left[-i(\omega_p t + k_p z)|i\rangle\langle i| - i(\omega_c t - k_c z + \ell_c\phi)|k\rangle\langle k|\right]. \tag{5}$$

Also, we shift the zero point of the energy to the ground-state hyperfine level indicated by the index, i, using

$$\hat{U}_2 = \hat{I}\exp\left[i(\omega_p + \omega_i)t\right]. \tag{6}$$

The transformed Hamiltonian is given by [39]

$$\hat{H}' = \hat{U}\hat{H}\hat{U}^\dagger + i\hbar\frac{\partial\hat{U}}{\partial t}\hat{U}^\dagger, \tag{7}$$

and the density matrix operator is transformed according to $\hat{\rho}' = \hat{U}\rho\hat{U}^\dagger$. Applying the rotating wave approximation to the transformed Hamiltonian from Eq. (7), we arrive at the following

Table 2
The mode, configuration, $\Omega_{0c,kl}$, and linewidth for EIT experiments in ^{85}Rb. The final column gives the theoretically predicted FWHM of the EIT signal if the control laser is in the opposite mode given in the first column, but same $\Omega_{0c,kl}$. Each configuration is described in Fig. 2.

Mode	Config.	$\Omega_{0c,kl}$ (MHz)	FWHM	Predicted FWHM (for opposite mode)
LG_0^1	(I)	16	0.67Γ	1.46Γ
	(II)	19	0.78Γ	1.87Γ
Gaussian	(I)	9.5	0.73Γ	0.37Γ
	(II)	11	0.85Γ	0.41Γ

Table 3
The mode, configuration, $\Omega_{0c,kl}$, and linewidth for EIT experiments in ^{87}Rb. The final column gives the theoretically predicted FWHM of the EIT signal if the control laser is in the opposite mode given in the first column, but same $\Omega_{0c,kl}$. Each configuration is described in Fig. 2.

Mode	Config.	$\Omega_{0c,kl}$ (MHz)	FWHM	Predicted FWHM (for opposite mode)
LG_0^1	(I)	20	0.8Γ	1.94Γ
	(II)	25	0.95Γ	2.64Γ
	(III)	33	1.5Γ	4.26Γ
	(IV)	33	1.2Γ	3.52Γ
Gaussian	(I)	7.3	0.46Γ	0.25Γ
	(II)	5.0	0.44Γ	0.22Γ
	(III)	6.9	0.61Γ	0.29Γ
	(IV)	8.2	0.75Γ	0.36Γ

full Hamiltonian for our system:

$$\hat{H}' = (-1)^k\hbar\left(\Delta_p - \Delta_c\right)|k\rangle\langle k| - \hbar\Delta_p|l\rangle\langle l| - \sum_{j=i+2,j\neq l}^{i+4}\hbar\left(\Delta_p + \omega_{il} - \omega_{ij}\right) + \frac{1}{2}\sum_{j=i+2}^{i+4}\hbar\Omega_{p,ij}(|i\rangle\langle j| + |j\rangle\langle i|) + \frac{1}{2}\hbar\Omega_{c,kl}(|k\rangle\langle l| + |l\rangle\langle k|), \tag{8}$$

where $\Delta_p = \omega_p - \omega_{il}$ and $\Delta_c = \omega_c - \omega_{kl}$.

The time evolution of the density matrix is governed by the Liouville–von Neumann equation [39]:

$$i\hbar\frac{\partial\hat{\rho}'}{\partial t} = \left[\hat{H}', \hat{\rho}'\right] + \hat{\mathcal{L}} + \hat{\mathcal{L}}_d, \tag{9}$$

where primes indicate a transformed operator, $\hat{\mathcal{L}}$ is an operator describing the losses in the system, and $\hat{\mathcal{L}}_d$ describes the dephasing due to the linewidth of the probe and control lasers. We build the loss operator in a similar fashion to [1]

$$\hat{\mathcal{L}} = \frac{1}{2}\sum_{j=i+2}^{i+3}\Gamma_{ji}\left[2|i\rangle\langle j|\hat{\rho}'|j\rangle\langle i| - |j\rangle\langle j|\hat{\rho}' - \hat{\rho}'|j\rangle\langle j|\right] + \frac{1}{2}\sum_{m=4}^{5}\Gamma_{mk}\left[2|k\rangle\langle m|\hat{\rho}'|m\rangle\langle k| - |m\rangle\langle m|\hat{\rho}' - \hat{\rho}'|m\rangle\langle m|\right], \tag{10}$$

where Γ_{ji} is the spontaneous decay rate from state j to i. The decoherence induced by the finite linewidth of the laser is given by [7,40]

$$\hat{\mathcal{L}}_d = -\sum_{m=1}^{6}\sum_{n=1}^{6}\gamma_{mn}|m\rangle\langle m|\hat{\rho}'|n\rangle\langle n|, \tag{11}$$

where the dephasing rate, γ_{mn}, is the sum of the relevant laser linewidths connecting state $|m\rangle$ to $|n\rangle$. If we let γ_p and γ_c be the linewidths of the probe and control lasers respectively, the dephasing rates are

$$\gamma_{i,i+2} = \gamma_{i+2,i} = \gamma_{i,i+3} = \gamma_{i+3,i} = \gamma_{i,i+4} = \gamma_{i+4,i} = \gamma_p,\ \gamma_{kl} = \gamma_{lk} = \gamma_c,\ \gamma_{12} = \gamma_{21} = \gamma_p + \gamma_c. \tag{12}$$

All other dephasing rates are zero due to electric dipole selection rules.

We make two more assumptions in our model. The first is that the system is in steady state, which gives $\partial\hat{\rho}'/\partial t = 0$. The second is that the probe laser is significantly weaker than the control laser. In this approximation, the density matrix elements ($\rho'_{nm} = \langle n|\hat{\rho}'|m\rangle$) simplify: $\rho'_{ii} \approx 1$, $\rho'_{nn} = 0$ for $n \neq i$, and $\rho'_{n,n+1} = \rho'_{n+1,n} = 0$ for $n = 1 \ldots 5$. Applying these assumptions and solving Eq. (9) for the off-diagonal density matrix elements associated with the three dipole-allowed transitions for the probe give

$$\rho'_{il}(r) = \frac{\frac{1}{2}\Omega_{p,il}(r)\left(\Delta_p - \Delta_c - i(\gamma_p + \gamma_c)\right)}{\left(\Delta_p - \frac{i}{2}(\Gamma_{li} + \Gamma_{lk} + 2\gamma_p)\right)\left(\Delta_p - \Delta_c - i(\gamma_p + \gamma_c)\right) - \frac{1}{4}\Omega_{c,kl}^2(r)}$$

and $\rho'_{ij}(r)$

$$= \frac{\frac{1}{2}\Omega_{p,ij}(r)}{\Delta_p + \omega_{il} - \omega_{ij} - \frac{i}{2}(\Gamma_{ji} + 2\gamma_p)} \quad \text{for } j = i+2 \ldots i+4 \text{ and } j \neq l. \tag{13}$$

The density matrix elements, $\rho'_{ij}(r)$, corresponding to $j \neq l$ behave like two-level transitions. However, the presence of the strong control laser that couples state $|k\rangle$ to state $|l\rangle$ leads to an EIT feature in the density matrix element $\rho'_{il}(r)$. Mathematically, this comes from the Rabi frequency term, $\Omega_{c,kl}(r)$, that appears in the expression for ρ'_{il} in Eq. (13). The r-dependence of the density matrix results from the spatial variation of the Rabi frequency. However,

for our system, this dependence is only relevant in the cases involving a control in the LG_0^1 mode.

Our experiment detects the transmission of a weak probe passing through a medium described by the six level model presented above. Using a semi-classical model, the induced electric dipole moment is given by [39]

$$p(r) = N \sum_{j=i+2}^{i+4} d_{ij}\left(\rho'_{ij}(r)\right)^* = \epsilon_0 \chi(r) \mathcal{E}_p(r), \tag{14}$$

where N is the number density of the atomic ensemble which we approximate to be constant, and $\chi(r)$ is the susceptibility. From Eq. (14), the susceptibility is given by

$$\chi(r) = \frac{N}{\epsilon_0 \mathcal{E}_p(r)} \sum_{j=i+2}^{i+4} d_{ij}\left(\rho'_{ij}(r)\right)^* = -\frac{N}{\epsilon_0 \hbar} \sum_{j=i+2}^{j+4} \frac{d_{ij}^2\left(\rho'_{ij}(r)\right)^*}{\Omega_{p,ij}(r)}. \tag{15}$$

The imaginary part of the susceptibility describes the absorption of the laser passing through the medium. Applying Beer's Law to determine the transmitted fraction of the probe laser

$$T = \frac{\int_0^{w_{0,p}} I_{0,p}(r) e^{-\mathrm{OD}(r)} r\, dr}{\int_0^{w_{0,p}} I_{0,p}(r) r\, dr} = \frac{2}{w_{0,p}^2} \int_0^{w_{0,p}} \exp(-\mathrm{Im}\left[\chi(r)\right] k_p z) r\, dr, \tag{16}$$

where $\mathrm{OD}(r) = \mathrm{Im}\left[\chi(r)\right] k_p z$ is the optical density, z is the length of the atomic medium along the propagation direction, and the probe laser is assumed to be a plane-wave. We let $z = 4$ mm, which is the $1/e^2$ diameter of the MOT. We integrate over the region of the EIT interaction, which we take to be a circle with a radius equal to the waist of the probe laser. We fit Eq. (16) to our data using $\Omega_{0c,kl}$, γ_p, γ_c, Δ_c, and N as fitting parameters. The width of the EIT feature is determined from the model by measuring the full-width at half-max (FWHM).

As a demonstration of the model, theoretical spectra for configuration (I) are shown for ^{85}Rb in Fig. 3(a) and for ^{87}Rb in Fig. 3 (b). The dashed blue curve is a theoretical spectrum when the control laser is in the LG_0^1 mode, and the solid red curve is a theoretical spectrum when the control laser is in the Gaussian mode. For all curves, we assume the control Rabi frequency constant to be $\Omega_{0c,kl} = 20$ MHz, the control laser linewidth to be $\gamma_c = 1$ MHz, the probe laser linewidth to be $\gamma_p = 0.1$ MHz, the number density to be $N = 5 \times 10^{10}$ cm^{-3}, and the control laser detuning to be $\Delta_c = 0$. Our model agrees with previous results [29] that for control lasers with equal $\Omega_{0c,kl}$, EIT involving a control laser in the LG_0^1 mode results in a narrowing of the resonance feature.

4. Results

Spectra for all four EIT configurations are measured for ^{87}Rb, and configurations (I) and (II) are measured for ^{85}Rb. Fig. 4 (a) shows a measurement of the EIT spectra of ^{85}Rb when the control is in the LG_0^1 mode, and Fig. 4(b) shows the same measurement with the control in the Gaussian mode. A best fit from the model is also shown in Fig. 4(a) and (b). The control laser is locked near the $|F = 3\rangle \rightarrow |F' = 2\rangle$ hyperfine transition, while the probe scans over the $|F = 2\rangle \rightarrow |F' = 1, 2, 3\rangle$ dipole allowed transitions. The EIT feature occurs in the $|F = 2\rangle \rightarrow |F' = 2\rangle$ transmission peak, which corresponds to configuration (I) in Fig. 2. We find excellent agreement between the model and data. We determine the EIT characteristics from the model. In Fig. 4(a), the control laser is in the LG_0^1 mode with $\Omega_{0c,32} = 16$ MHz, and the laser frequency is 1.4 MHz above the $|F = 3\rangle \rightarrow |F' = 2\rangle$ transition. The FWHM of the EIT feature is 0.67Γ, where $\Gamma = 2\pi \times 6.07$ MHz. In Fig. 4(b), the control laser is in the Gaussian mode with $\Omega_{0c,32} = 9.5$ MHz, and the laser frequency is 1.8 MHz below the $|F = 3\rangle \rightarrow |F' = 2\rangle$ transition. The FWHM of the EIT feature is 0.73Γ. The different values for the control laser frequency detuning are due to a drift in the lock of the control laser.

Fig. 5(a) shows a measurement of the EIT spectra of ^{87}Rb when the control is in the LG_0^1 mode, and Fig. 5(b) shows the same measurement with the control in the Gaussian mode. A best corresponding fit from the model is also shown in Fig. 5(a) and (b). The control laser is locked near the $|F = 2\rangle \rightarrow |F' = 1\rangle$ hyperfine transition, while the probe scans over the $|F = 1\rangle \rightarrow |F' = 0, 1, 2\rangle$ dipole allowed transitions. The EIT feature occurs in the $|F = 1\rangle \rightarrow |F' = 1\rangle$ transmission peak, which corresponds to configuration (I) in Fig. 2. We again determine the EIT characteristics from the fit. In Fig. 5 (a), the control laser is in the LG_0^1 mode with $\Omega_{0c,21} = 20$ MHz, and the laser frequency is 0.1 MHz below the $|F = 2\rangle \rightarrow |F' = 1\rangle$ transition. The FWHM of the EIT feature is 0.8Γ. In Fig. 5(b), the control laser is in the Gaussian mode with $\Omega_{0c,21} = 9.5$ MHz, and the laser frequency is 0.7 MHz above the $|F = 2\rangle \rightarrow |F' = 1\rangle$ transition. The FWHM of the EIT feature is 0.46Γ. Again, there is excellent agreement between experiment and theory.

We make similar measurements on the other configurations in Fig. 2. The results for ^{85}Rb are found in Table 2, and the results for ^{87}Rb are in Table 3. For ^{85}Rb, the observed EIT linewidths are the same, but $\Omega_{0c,kl}$ for the control laser for the LG_0^1 system is 70% larger. The larger intensity is necessary to achieve sufficient signal. Increasing the intensity of the Gaussian control laser for direct comparison would lead to an additional feature in the transmission profile due to effects coming from the degenerate Zeeman sublevels not included in our model [41]. For ^{87}Rb, the EIT linewidths we observe are a factor of two larger than those with a Gaussian control beam, but the corresponding values of $\Omega_{0c,kl}$ are 2.5–5 times larger. We also used our model to investigate the predicted linewidths of the EIT for the opposite control mode with same $\Omega_{0c,kl}$ (shown in the final column of Tables 2 and 3). The measured linewidths of a configuration with a given $\Omega_{0c,kl}$ in the LG_0^1 mode are narrower than the predicted linewidths of the identical configuration with the control in the Gaussian mode. Similarly, the predicted linewidths of a configuration with a given $\Omega_{0c,kl}$ of the control in the LG_0^1 mode are narrower than the measured linewidths of the identical configuration with the control in the Gaussian mode.

Given these results and the quality of the fit of the model (Figs. 4 and 5), both for LG_0^1 and Gaussian control lasers, we conclude that the linewidth is narrower with the LG_0^1 control beam for equal $\Omega_{0c,kl}$ in an ultracold gas. Because the atoms travel ~10 μm during the experiment, the effect is independent of the transit time of the atoms. This is consistent with what has previously been observed in gases at room temperature where it was shown to be independent of the OAM of the control beam [28,29].

5. Conclusion

We observe EIT transmission spectra using a control beam in an LG_0^1 laser mode in ultracold atoms prepared in a magneto-optical trap. We measure EIT linewidths with the control beam in the LG_0^1 mode, and compare to the spectra generated when the control beam is in the Gaussian mode. In both mode types, we observe sub-natural linewidths with similar signal contrast. Our theoretical model for this system shows good agreement with the experiment. We conclude that EIT in an ultracold gas results in a narrower resonance feature for the same value of $\Omega_{0c,kl}$ when a control beam is in an LG_0^1 mode as compared to the control beam in a Gaussian mode. Decoherences due to transit effects are negligible.

Therefore, we conclude that the narrowing of the EIT resonance feature is due to the spatial variation of the Rabi frequency of a control laser in the LG_0^1 mode.

Acknowledgments

This project is funded by The Research Corporation under grant number RI0316. We would like to acknowledge the constructive conversations with Michael A. Morrison regarding the development of the theoretical model.

References

[1] M. Fleischhauer, A. Imamoglu, J.P. Marangos, Electromagnetically induced transparency: optics in coherent media, Rev. Mod. Phys. 77 (2005) 633–673. http://dx.doi.org/10.1103/RevModPhys.77.633.
[2] C. Liu, Z. Dutton, C.H. Behroozi, L.V. Hau, Observation of coherent optical information storage in an atomic medium using halted light pulses, Nature 409 (6819) (2001) 490–493.
[3] D.F. Phillips, A. Fleischhauer, A. Mair, R.L. Walsworth, M.D. Lukin, Storage of light in atomic vapor, Phys. Rev. Lett. 86 (2001) 783–786. http://dx.doi.org/10.1103/PhysRevLett.86.783.
[4] S.E. Harris, J.E. Field, A. Imamoglu, Nonlinear optical processes using electromagnetically induced transparency, Phys. Rev. Lett. 64 (1990) 1107–1110. http://dx.doi.org/10.1103/PhysRevLett.64.1107.
[5] G.S. Agarwal, Inhibition of spontaneous emission noise in lasers without inversion, Phys. Rev. Lett. 67 (1991) 980–982. http://dx.doi.org/10.1103/PhysRevLett.67.980.
[6] K.-J. Boller, A. Imamolu, S.E. Harris, Observation of electromagnetically induced transparency, Phys. Rev. Lett. 66 (1991) 2593–2596. http://dx.doi.org/10.1103/PhysRevLett.66.2593.
[7] J. Gea-Banacloche, Y.-q. Li, S.-z. Jin, M. Xiao, Electromagnetically induced transparency in ladder-type inhomogeneously broadened media: theory and experiment, Phys. Rev. A 51 (1995) 576–584. http://dx.doi.org/10.1103/PhysRevA.51.576.
[8] A.J. Olson, S.K. Mayer, Electromagnetically induced transparency in rubidium, Am. J. Phys. 77 (2009) 116–121.
[9] S. Mitra, M. Hossain, B. Ray, P. Ghosh, S. Cartaleva, D. Slavov, On line shape of electromagnetically induced transparency in a multilevel system, Opt. Commun. 283 (7) (2010) 1500–1509, doi: http://dx.doi.org/10.1016/j.optcom.2009.11.088.
[10] S.R. Chanu, A.K. Singh, B. Brun, K. Pandey, V. Natarajan, Subnatural linewidth in a strongly-driven degenerate two-level system, Opt. Commun. 284 (20) (2011) 4957–4960, doi: http://dx.doi.org/10.1016/j.optcom.2011.07.001.
[11] S. Hopkins, E. Usadi, H. Chen, A. Durrant, Electromagnetically induced transparency of laser-cooled rubidium atoms in three-level λ-type systems, Opt. Commun. 138 (1–3) (1997) 185–192, doi: http://dx.doi.org/10.1016/S0030-4018(97)00030-8.
[12] M. Yan, E.G. Rickey, Y. Zhu, Electromagnetically induced transparency in cold rubidium atoms, J. Opt. Soc. Am. B 18 (8) (2001) 1057–1062. http://dx.doi.org/10.1364/JOSAB.18.001057.
[13] J. Wang, Y. Zhu, K.J. Jiang, M.S. Zhan, Bichromatic electromagnetically induced transparency in cold rubidium atoms, Phys. Rev. A 68 (2003) 063810. http://dx.doi.org/10.1103/PhysRevA.68.063810.
[14] K. Kowalski, V.C. Long, H.N. Viet, S. Gateva, M. Głódź, J. Szonert, Simultaneous coupling of three hfs components in a cascade scheme of EIT in cold ^{85}Rb atoms, J. Non-Cryst. Solids 355 (24–27) (2009) 1295–1301, doi: http://dx.doi.org/10.1016/j.jnoncrysol.2009.05.033.
[15] V.B. Tiwari, S. Singh, H.S. Rawat, M.P. Singh, S.C. Mehendale, Electromagnetically induced transparency in cold ^{85}Rb atoms trapped in the ground hyperfine $F = 2$ state, J. Phys. B: At. Mol. Opt. Phys. 43 (9) (2010) 095503.
[16] L.V. Hau, S.E. Harris, Z. Dutton, C.H. Behroozi, Light speed reduction to 17 metres per second in an ultracold atomic gas, Nature 3970 (672) (1999) 594–598.
[17] D. Budker, D.F. Kimball, S.M. Rochester, V.V. Yashchuk, Nonlinear magneto-optics and reduced group velocity of light in atomic vapor with slow ground state relaxation, Phys. Rev. Lett. 83 (1999) 1767–1770. http://dx.doi.org/10.1103/PhysRevLett.83.1767.
[18] M.M. Kash, V.A. Sautenkov, A.S. Zibrov, L. Hollberg, G.R. Welch, M.D. Lukin, Y. Rostovtsev, E.S. Fry, M.O. Scully, Ultraslow group velocity and enhanced nonlinear optical effects in a coherently driven hot atomic gas, Phys. Rev. Lett. 82 (1999) 5229–5232. http://dx.doi.org/10.1103/PhysRevLett.82.5229.
[19] G. Molina-Terriza, J.P. Torres, L. Torner, Twisted photons, Nat. Phys. 3 (2007) 305.
[20] R. Pugatch, M. Shuker, O. Firstenberg, A. Ron, N. Davidson, Topological stability of stored optical vortices, Phys. Rev. Lett. 98 (2007) 203601. http://dx.doi.org/10.1103/PhysRevLett.98.203601.
[21] P.K. Vudyasetu, R.M. Camacho, J.C. Howell, Storage and retrieval of multimode transverse images in hot atomic rubidium vapor, Phys. Rev. Lett. 100 (2008) 123903. http://dx.doi.org/10.1103/PhysRevLett.100.123903.
[22] T. Wang, L. Zhao, L. Jiang, S.F. Yelin, Diffusion-induced decoherence of stored optical vortices, Phys. Rev. A 77 (2008) 043815. http://dx.doi.org/10.1103/PhysRevA.77.043815.
[23] O. Firstenberg, P. London, D. Yankelev, R. Pugatch, M. Shuker, N. Davidson, Self-similar modes of coherent diffusion, Phys. Rev. Lett. 105 (2010) 183602. http://dx.doi.org/10.1103/PhysRevLett.105.183602.
[24] R. Inoue, N. Kanai, T. Yonehara, Y. Miyamoto, M. Koashi, M. Kozuma, Entanglement of orbital angular momentum states between an ensemble of cold atoms and a photon, Phys. Rev. A 74 (2006) 053809. http://dx.doi.org/10.1103/PhysRevA.74.053809.
[25] D. Moretti, D. Felinto, J.W.R. Tabosa, Collapses and revivals of stored orbital angular momentum of light in a cold-atom ensemble, Phys. Rev. A 79 (2009) 023825. http://dx.doi.org/10.1103/PhysRevA.79.023825.
[26] L. Veissier, A. Nicolas, L. Giner, D. Maxein, A.S. Sheremet, E. Giacobino, J. Laurat, Reversible optical memory for twisted photons, Opt. Lett. 38 (5) (2013) 712–714. http://dx.doi.org/10.1364/OL.38.000712.
[27] A. Nicolas, L. Veissier, L. Giner, E. Giacobino, D. Maxein, J. Laurat, A quantum memory for orbital angular momentum photonic qubits, Nat. Photonics 8 (3) (2014) 234–238.
[28] J. Anupriya, N. Ram, M. Pattabiraman, Hanle electromagnetically induced transparency and absorption resonances with a Laguerre Gaussian beam, Phys. Rev. A 81 (2010) 043804. http://dx.doi.org/10.1103/PhysRevA.81.043804.
[29] S.R. Chanu, V. Natarajan, Narrowing of resonances in electromagnetically induced transparency and absorption using a Laguerre–Gaussian control beam, Opt. Commun. 295 (2013) 150–154, doi: http://dx.doi.org/10.1016/j.optcom.2013.01.042.
[30] R. Kapoor, G.S. Agarwal, Theory of electromagnetically induced waveguides, Phys. Rev. A 61 (2000) 053818. http://dx.doi.org/10.1103/PhysRevA.61.053818.
[31] S.A. Kennedy, G.W. Biedermann, J.T. Farrar, T.G. Akin, S.P. Krzyzewski, E.R. I. Abraham, Confinement of ultracold atoms in a Laguerre–Gaussian laser beam created with diffractive optics, Opt. Commun. 321 (2014) 110–115, doi: http://dx.doi.org/10.1016/j.optcom.2014.01.084.
[32] C.E. Wieman, L. Hollberg, Using diode lasers for atomic physics, Rev. Sci. Instrum. 62 (1) (1991) 1–20. http://dx.doi.org/10.1063/1.1142305.
[33] A. Millett-Sikking, I.G. Hughes, P. Tierney, S.L. Cornish, DAVLL lineshapes in atomic rubidium, J. Phys. B: At. Mol. Opt. Phys. 40 (1) (2007) 187.
[34] S.A. Kennedy, M.J. Szabo, H. Teslow, J.Z. Porterfield, E.R.I. Abraham, Creation of Laguerre–Gaussian laser modes using diffractive optics, Phys. Rev. A 66 (2002) 043801. http://dx.doi.org/10.1103/PhysRevA.66.043801.
[35] D. Bhattacharyya, B. Ray, P.N. Ghosh, Theoretical study of electromagnetically induced transparency in a five-level atom and application to Doppler-broadened and Doppler-free Rb atoms, J. Phys. B: At. Mol. Opt. Phys. 40 (20) (2007) 4061.
[36] D.A. Steck, Rubidium 85 D line data [online]. Available online at ⟨http://steck.us/alkalidata⟩.
[37] D.A. Steck, Rubidium 87 D line data [online]. Available online at ⟨http://steck.us/alkalidata⟩.
[38] L. Allen, M.W. Beijersbergen, R.J.C. Spreeuw, J.P. Woerdman, Orbital angular momentum of light and the transformation of Laguerre–Gaussian laser modes, Phys. Rev. A 45 (1992) 8185–8189. http://dx.doi.org/10.1103/PhysRevA.45.8185.
[39] D.A. Steck, Quantum and Atom Optics, 2014, available online at ⟨http://atomoptics.uoregon.edu/∼dsteck/teaching/quantum-optics/⟩.
[40] M. Tanasittikosol, J.D. Pritchard, D. Maxwell, A. Gauguet, K.J. Weatherill, R. M. Potvliege, C.S. Adams, Microwave dressing of Rydberg dark states, J. Phys. B: At. Mol. Opt. Phys. 44 (18) (2011) 184020.
[41] Y.-C. Chen, C.-W. Lin, I.A. Yu, Roles of degenerate Zeeman levels in electromagnetically induced transparency, Phys. Rev. A 61 (2000) 053805. http://dx.doi.org/10.1103/PhysRevA.61.053805.